iScience

Article

ARL13B regulates juxtaposed cilia-cilia elongation in BBSome dependent manner in *Caenorhabditis elegans*

Graphical abstract

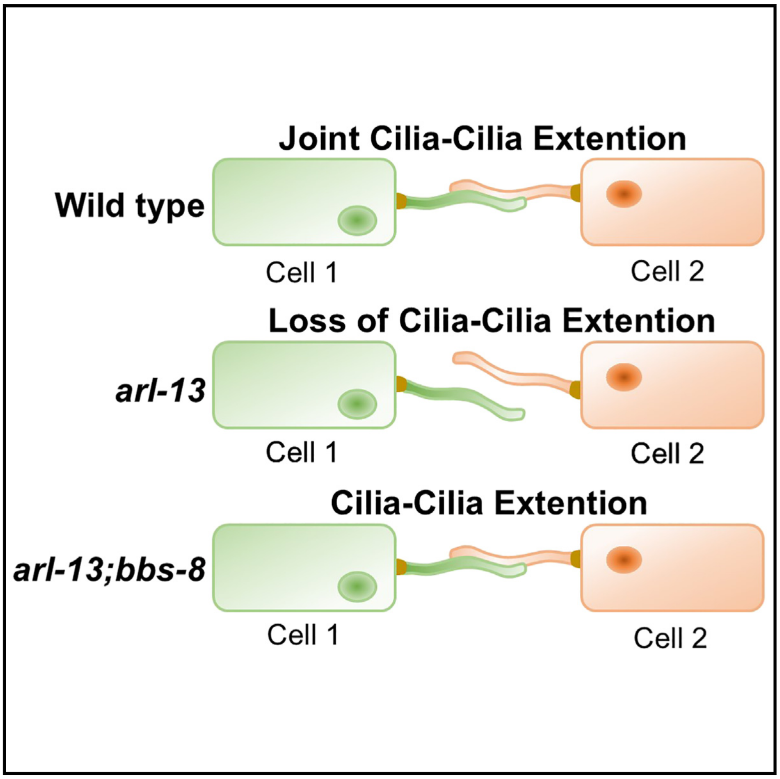

Highlights

- ARL-13 is crucial for juxtaposed cilia-cilia elongation (JCE)
- JCE is independent of cilia length
- NPHP2 along with HDAC-6 exacerbated the cilia misdirection phenotype in *ARL-13* mutants
- BBSome partially rescues JCE defect

Authors

Merve Gül Turan, Hanife Kantarci, Sebiha Cevik, Oktay I. Kaplan

Correspondence

sebiha.cevik@agu.edu.tr (S.C.),
oktay.kaplan@agu.edu.tr (O.I.K.)

In brief

Cell biology; Organizational aspects of cell biology; Functional aspects of cell biology

Turan et al., 2025, iScience *28*, 111791
February 21, 2025 © 2025 Published by Elsevier Inc.
https://doi.org/10.1016/j.isci.2025.111791

CellPress

iScience

CellPress
OPEN ACCESS

Article

ARL13B regulates juxtaposed cilia-cilia elongation in BBSome dependent manner in *Caenorhabditis elegans*

Merve Gül Turan,[1,2] Hanife Kantarci,[1] Sebiha Cevik,[1,*] and Oktay I. Kaplan[1,3,*]
[1]Rare Disease Laboratory, School of Life and Natural Sciences, Abdullah Gul University, Kayseri, Turkiye
[2]Department of Bioengineering, School of Life and Natural Sciences, Abdullah Gul University, Kayseri, Turkiye
[3]Lead contact
*Correspondence: sebiha.cevik@agu.edu.tr (S.C.), oktay.kaplan@agu.edu.tr (O.I.K.)
https://doi.org/10.1016/j.isci.2025.111791

SUMMARY

The interaction of cilia with various cellular compartments, such as axons, has emerged as a new form of cellular communication. Cilia often extend in proximity to cilia from neighboring cells. However, the mechanisms driving this process termed juxtaposed cilia-cilia elongation (JCE) remain unclear. We use fluorescence-based visualization to study the mechanisms of coordinated cilia elongation in sensory neurons of *Caenorhabditis elegans*. Conducting a selective gene-based screening strategy reveals that ARL-13/ARL13B and MKS-5/RPGRIP1L are essential for JCE. We demonstrate that ARL-13 modulates JCE independently of cilia length. Loss of NPHP-2/inversin along with HDAC-6 enhances the cilia misdirection phenotype of *arl-13* mutants, while disruption of the BBSome complex, but not microtubule components, partially suppresses the JCE defects in *arl-13* mutants. We further show changes in the phospholipid compositions in *arl-13* mutants. We suggest that ARL-13 contributes to JCE, in part, through the modulation of the ciliary membrane.

INTRODUCTION

Cilia are microscopic projections extending into the extracellular spaces from the cell surface, consisting of a microtubule (MT)-based core surrounded by the ciliary plasma membrane.[1] In humans, diverse cell types possess cilia, including those in the oviduct, nodes, lungs, ependymal cells, photoreceptors, kidney-collecting ducts, and sperm, each performing distinct functions based on cell type requirements.[2–4] For instance, olfactory cilia are located in the upper layer of the interior of the nasal passages, contributing to the perception of odorants through their tree-like cilia structure.[5,6] Ependymal cell cilia play crucial roles in circulating cerebrospinal fluid, while lung cell cilia assist respiratory processes by moving mucus.[7] The impaired functioning of cilia in human cells results in the manifestation of a variety of symptoms, giving rise to a spectrum of cilia-related rare diseases collectively known as ciliopathy.

The discovery of bidirectional movements of particles along flagella in *Chlamydomonas reinhardtii* in 1993 marked the identification of the intraflagellar transport (IFT) process.[8] IFT trains facilitate the transport of molecules in both anterograde (from the base to the tip) and retrograde (from the tip back to the base) directions and are essential for cilia formation and functionality.[9] The IFT system consists of two multisubunit complexes: IFT-A and IFT-B. IFT-A and IFT-B complexes are interconnected during anterograde and retrograde transports and driven by the dynein and kinesin-2 motors, respectively. In addition to the IFT-A and IFT-B complexes, the BBSome, an octameric complex, is associated with IFT molecules. Comprising eight subunits encoded by various BBS genes (BBS1, BBS2, BBS4, BBS5, BBS7, BBS8, BBS9, and BBS18), the BBSome connects IFT trains to the ciliary membrane.[10–13]

Cilia projections extend into extracellular spaces enabling them to establish connections with other cellular compartments, including axons and other cilia. A recent study has revealed the formation of synapses between the sensory cilium and axons of neurons.[14] In particular, cilia-cilia contacts have been observed in human cells.[15] Furthermore, in the nematode *Caenorhabditis elegans*, transmission electron microscopy (TEM) analysis has unveiled a bundle of cilia projecting in juxtaposition from the distal dendritic ends of sensory neurons, such as ASE, ASG, ASH, ASI, ASJ, ASK, ADF, and ADL,[16–19] in the amphid channel of the head. Additionally, cilia from PHA and PHB sensory neurons project side by side, establishing a Y-like structure in the tail phasmid in *C. elegans*.[20] While molecular mechanisms controlling the cilia length are well documented, the molecular mechanisms underlying the joint cilia elongation remain poorly characterized.

Here, we develop a fluorescence-based visualization technique designed to explore the mechanisms behind the projection of juxtaposed cilia-cilia in *C. elegans*, a phenomenon termed "juxtaposed cilia-cilia elongation" (JCE). These juxtaposed cilia, coordinated growth of neighboring cilia, originate from distinct sensory neurons in *C. elegans.* To explore the JCE mechanism, we assigned the term "normal" through paper to wild-type worm PHA and PHB and ASE and ASI cilia to describe their phenotype.

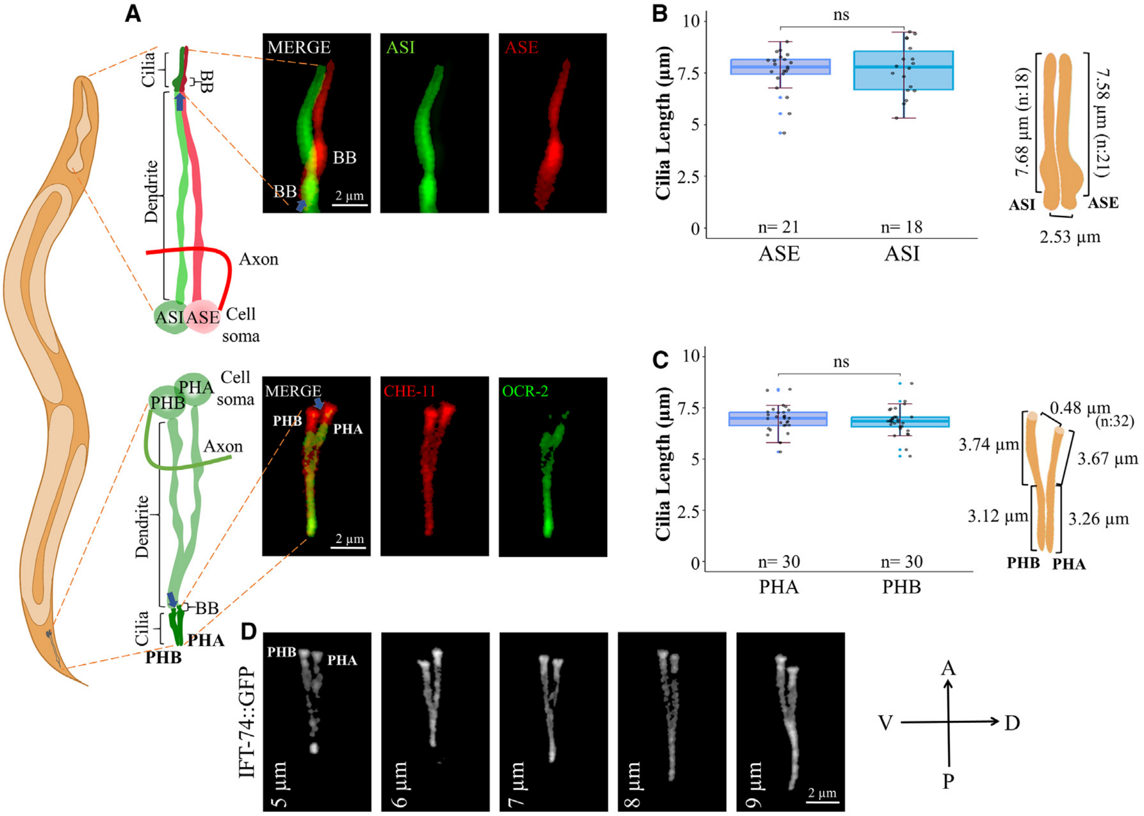

Figure 1. Fluorescence-based visualization of juxtaposed cilia-cilia elongation in *C. elegans*

(A) Shown is a whole worm displaying the positions of ciliated sensory neurons in both the head and tail. The schematic displays cell soma, axon, dendrite, cilia, and basal body (BB) for the ciliated sensory neurons ASE and ASI in the head and PHA and PHB in the tail. Gray arrows in schematic and *in vivo* fluorescent cilia photos point out the contact positions between both ASE and ASI and PHA and PHB cilia. Fluorescent markers (*gcy-5::mCherry* and *str-3::gfp*) are employed to visualize the cilia of ASE and ASI, respectively. The cilia of PHA and PHB were illustrated with CHE-11::mCherry (red) and OCR-2:eGFP (green) fluorescent markers. Scale bar: 2 μm.

(B and C) The average lengths of cilia for ASE and ASI and PHA and PHB were measured and depicted in the boxplot (shown in μm). The representative schematic displays the measurements for the ASE and ASI (*n* for ASE: 21, *n* for ASI: 18) and PHA and PHB (*n* for PHA: 30, *n* for ASI: 30). Distances between the periciliary membrane compartment (PCMC) of ASE and ASI cilia or PHA and PHB were shown with the mean and standard error of the mean (±SEM). The representative measurement for PHA and PHB cilia starts from the PCMC and extends to where two cilia first join, and the subsequent measurement shows beyond the region where two cilia meet. The Wilcoxon two-paired statistical test is utilized to compare the lengths of ASE and ASI and PHA and PHB cilia, where "*n*" denotes the number of measured cilia (ns indicates non-significance).

(D) Shown is the range of PHA and PHB cilia lengths visualized with endogenous IFT-74::GFP. PHA and PHB cilia exhibit variations in length even if they are the same age. In all wild types, the cilia converge at the midpoint and extend to the tip of the cilia, forming the Y-like structure. Scale bar: 2 μm. A stands for anterior, P for posterior, D for dorsal, and V for ventral orientation.

Furthermore, we used the term "misdirection" to characterize any phenotypically abnormal structures in PHA and PHB and ASE and ASI cilia. Here, using a targeted gene-based screening strategy, our findings reveal the indispensable roles of ARL-13/ARL13B and MKS-5/RPGRIP1L in JCE. Our genetic analyses reveal that ARL-13 affects JCE independently of cilia length. The loss of NPHP-2/inversin along with HDAC-6 increases the percentage of the cilia misdirection phenotypes in *arl-13* mutants. However, the disruption of the BBSome complex, but not stabilizing MT components partially suppresses the cilia misdirection phenotype in *arl-13* mutants. Additionally, our findings reveal alterations in phospholipid compositions in *arl-13* mutants. We propose that ARL-13 contributes to JCE, partly through the modulation of the ciliary membrane.

RESULTS

Fluorescence-based visualization of the JCE in head and tail sensory neurons of *C. elegans*

Here, we generate two-color fluorescence markers to visualize juxtaposed cilia extension in both the head and tails of *C. elegans*. We chose ASE and ASI cilia from the amphid channel cilia and labeled them red (*gcy-5::mCherry* for ASE) and green (*str-3::gfp* for ASI) to visualize the ASE and ASI cilia, respectively (Figure 1A). Similar to the serial section transmission electron microscopy (ssTEM),[16,19] our microscopy images revealed that the cilia of ASE and ASI extend in the same direction by juxtaposition (Figure 1A). The periciliary membrane compartment (PCMC) of ASE and ASI is differently positioned, and the distance between

PCMCs of ASE and ASI is 2.53 μm; however, the rod-shaped cilia of ASE and ASI have comparable cilia lengths (Figures 1B and 1C).

Next, we imaged the length of PHA and PHB cilia, and the individual cilia of PHA and PHB converged at the midpoint. The distance from the basal bodies (BBs) to the intersection point was measured to be 3.67 μm for PHA cilium and 3.74 μm for PHB cilium, while the distance from the intersection point to the tip of the cilium was measured to be 3.26 μm for PHA cilium and 3.12 μm for PHB cilium. These PHA and PHB cilia form a Y-like structure (Figures 1D–1F; Video S1). Furthermore, our measurement reveals that the distance between BBs of PHA and PHB cilia is 0.48 μm (Figure 1F). Even though the cilia length of PHA/PHB varies in wild-type, the Y-like structure of PHA/PHB cilia is maintained across various cilia lengths (5–9 μm) (Figure 1G). Furthermore, the Y-like structure does not alter as the worm ages (from the larval stage 4 to day 8) (Figure S1). We term this process "JCE." Taken together, our work establishes an *in vivo* fluorescence-based system to monitor the JCE of different cilia types in *C. elegans.*

JCE of PHA and PHB and ASE and ASI cilia elongation requires Joubert syndrome-associated ARL-13

Our *in vivo* fluorescence-based system facilitates the screening analysis for genes associated with defects in JCE, thus we conduct a selective gene-based screening strategy. We specifically seek mutants that differ significantly from the wild-type by failing to extend cilia side by side (Figure 2A). We chose PHA/PHB cilia (Y-like cilia) for the screening process because the tail is less mobile and, thus, easier to take live images for screening. For screening, we pick 23 genes that encode proteins localizing to cilia (CEP-104,[21] KAP-1,[22] HDAC-6,[23] KLP-13,[22] NPHP-2,[24] DYF-5,[25] TTLL-4,[26] BBS-5,[27,28] BBS-7,[29] and RPI-1[30]), transition zone (TZ)/BB (MKS-2,[31] NPHP-4,[32] MKSR-1,[33] MKS-5,[34] MKS-6,[35] CCEP-290,[36] CDKL-1,[37] ELMD-1[38] and WDR-31,[38] and TTLL-11[39]), an NEKL-4 kinase associated with cilia function[40,41] and the ciliary membrane (ARL-13).[42] WDR-54 was included in the screening analysis since it is a newly discovered cilia gene.[43]

We obtain/generate all these mutants and use confocal microscopy to screen mutants for the failure of Y-like cilia to join together. Similar to the merging of PHA and PHB cilia in the middle of the cilia and joint extension of the distal segment of the cilia in the wild-type, the Y-like cilia structure of PHA/PHB cilia in 20 different mutants remains undisrupted, which we labeled "normal phenotype." In contrast, *mks-5(tm3100)* (the human RPGRIP1L ortholog), *dyf-5(ok1177)* (the human ICK/CILK1 ortholog), and *arl-13(gk513)* (the human ARL13B ortholog) single mutants display abnormal Y-like cilia (Figure 2A). In particular, we identify diverse phenotypes, including the non-joining of the ciliary tip in PHA and PHB, and the directional turning of PHA and PHB cilia, yet we did not observe the backward rotation of the cilia in any of these mutants. All of these phenotypes are referred to as the "cilia misdirection phenotype" (Figure S2). We quantify the phenotypes of PHA and PHB cilia in wild-type and all 23 mutants, using "normal" and "misdirection" phenotypic classifications in our analysis (Figure 2B). Our microscopic quantification analysis reveals that only the *mks-5* and *arl-13* single mutants exhibit a statistically significant cilia misdirection phenotype (0% for wild-type vs. 21.05% for *mks-5(tm3100)* and 57.41% for *arl-13(gk513)*) (Figure 2B). The cilia misdirection phenotype in these mutants could be owing to disproportionate cilia elongation in PHA and PHB, thus we measured the PHA and PHB cilia length in all mutants tested (Figure 2C). Surprisingly, our findings reveal that the lengths of the cilia in *arl-13* mutants are similar to those of the wild-type, with no differences between the lengths of PHA and PHB cilia in *arl-13* and *mks-5(tm3100)* mutants (Figures 2C–2E). These findings suggest excessive cilia elongation cannot account for the observed cilia misdirection phenotype.

We generated *mks-5;arl-13* double mutants to assess the impact on cilia misdirection, but found no significant enhancement compared to *arl-13* single mutants (Figures S3A–S3C). Because the portion of cilia misdirection phenotype is higher for *arl-13(gk513)* without negatively affecting the cilia length, subsequent analysis of *arl-13*(gk513) mutants is needed to find out whether the other cilia types will exhibit the cilia misdirection phenotype and whether the cilia misdirection phenotype is independent of cilia length. Thus, in wild-type and *arl-13(gk513)* mutants, we monitor and quantify the juxtaposed extension of ASE and ASI cilia (Figure 3A). We observe a significant fraction of ASE and ASI cilia misdirected phenotype in the *arl-13(gk513)* single mutant compared to the wild-type, despite comparable cilia length. (Figures 3B–3D). Next, we introduce a transgene expressing ARL-13 driven by the *arl-13* promoter into the *arl-13(gk513)* mutant strain, with CHE-11::mCherry employed to visualize cilia. This exogenous expression of ARL-13 completely rescues the misdirection phenotype of PHA/PHB cilia (Figures 3E and 3F). These results indicate that *mks-5/RPGRIP1L* and *arl-13/ARL13B* are both required for the juxtaposed elongation of cilia. Our findings not only enhance our understanding of the basic mechanisms underlying ciliary misdirection but also highlight the role of *arl-13* and *mks-5* in this process.

Cilia length and JCE are independent of each other

We next investigated whether cilia extension and JCE are independent processes by selecting genes with established roles in cilia elongation. Specifically, we examined *cdkl-1* (the ortholog of human CDKL5), *dyf-5* (the ortholog of human ICK/CILK1), and *nekl-4* (the ortholog of human NEK10), each of which has been implicated in regulating cilia length.[22,37,44,45] Meanwhile, the loss of *nekl-4* in *osm-3(sa125)* mutant (the ortholog of human KIF17) causes the suppression of the ciliary phenotype.[46] We created double mutants, *cdkl-1; arl-13, dyf-5;arl-13*, and *nekl-4;arl-13*, and assessed the length of PHA and PHB cilia while quantifying the cilia misdirection phenotype in PHA/PHB cilia (Figures 4A, S4A, and S4B). Although the PHA and PHB cilia lengths in these double mutants were either extended or shortened, the percentage of their cilia misdirection phenotypes resembled those of *arl-13* single mutants (Figure 4B).

Blacque and his colleagues previously demonstrated that the *mks-2;ift-139* double mutants exhibit a cilia misdirection phenotype.[47] We generated the same double mutant for further analysis, and our microscopy analysis reveals a 7.84% incidence of misdirection in *mks-2;ift-139* mutants, compared to 0% in either single mutant (Figure 4A). To assess whether these genes enhance the cilia misdirection phenotype in *arl-13* mutants, we create

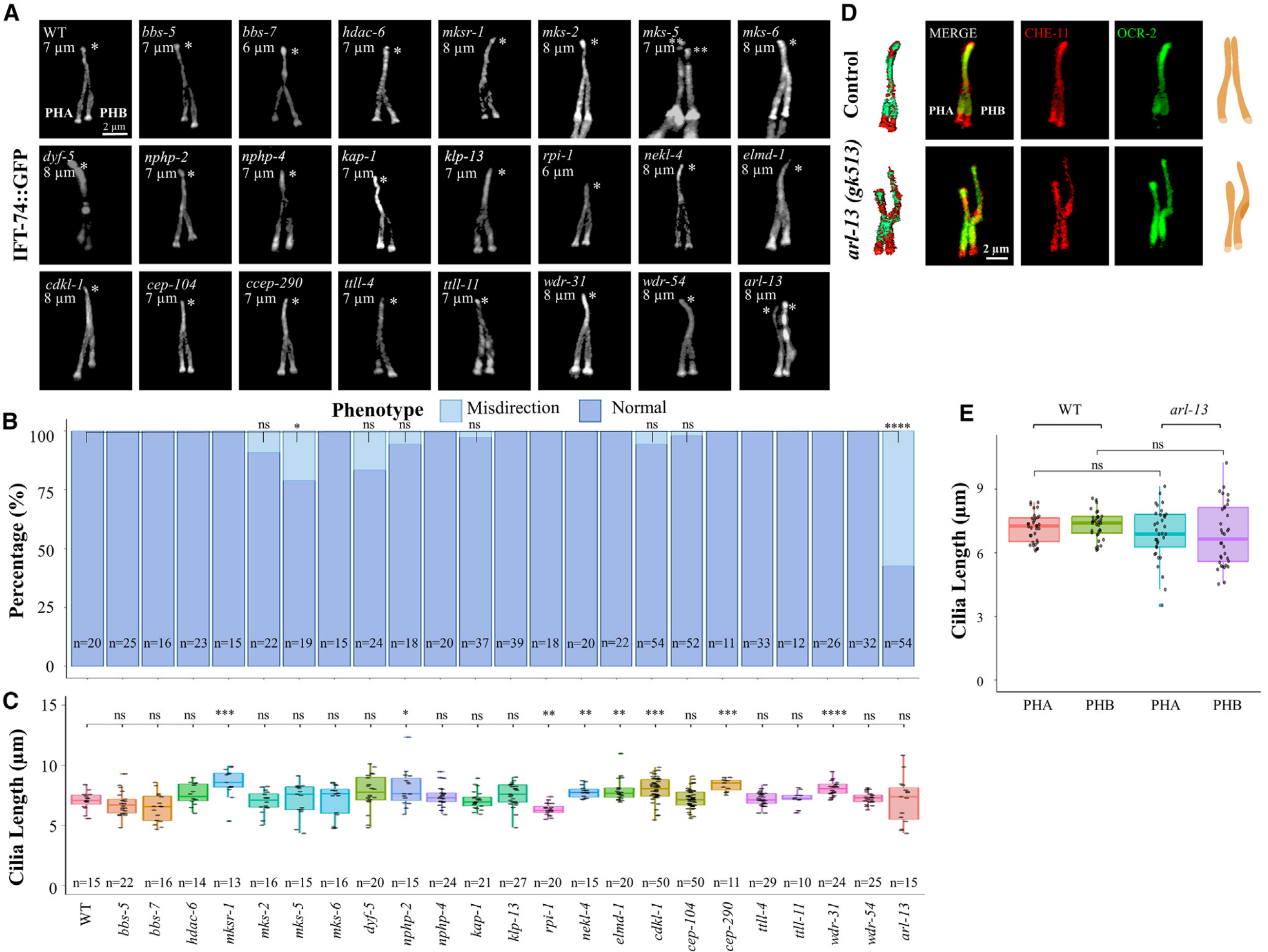

Figure 2. ARL-13 is required for the juxtaposed cilia-cilia elongation (JCE) of PHA and PHB

(A) Images depict PHA and PHB cilia in wild-type and 23 indicated single mutants. Fluorescent markers, including single-copy OSM-6::GFP and endogenous single-copy IFT-74::GFP, were used to visualize the PHA and PHB cilia. The cilia length depicted in the images corresponds to the respective cilia shown in the images. The asterisk (*) indicates the ciliary tip in PHA and PHB cilia. Scale bar: 2 µm.

(B) Stack bar charts display the percentage of normal cilia and misdirection cilia phenotype for PHA and PHB cilia in wild-type and indicated single mutants. Fisher's exact test compares statistical significance between wild-type and indicated mutants (ns = not significant, * = 0.05, **** = 0.0001). "*n*" denotes the number of measured cilia for each mutant.

(C) PHA cilia lengths for wild-type and indicated mutants are shown along with the mean. Wilcoxon paired-two statistical test was used for statistical analysis (ns = not significant, * = 0.05, ** = 0.01, *** = 0.001, **** = 1e-04).

The number of PHA and PHB cilia counted for each mutant is denoted as "*n*" for (B) and (C).

(D) Images display PHA and PHB cilia for wild-type and *arl-13(gk513)* mutants. Fluorescent markers CHE-11::mCherry (red) and OCR-2:eGFP (green) were used to visualize the PHA and PHB cilia. The representative schematics are shown next to fluorescent images. Scale bar: 2 µm.

(E) Cilia lengths of PHA and PHB, tagged with endogenous single-copy IFT-74::GFP, are displayed for both wild-type and *arl-13(gk513)* mutants along with the mean. Wilcoxon paired-two test compares cilia lengths (ns = not significant).

arl-13;mks-2 and *arl-13;ift-139* double mutants. Quantification reveals misdirection rates of 52.63% and 45.45% in *arl-13;mks-2* and *arl-13;ift-139* mutants, respectively, indicating that the cilia misdirection phenotype in *arl-13* single mutants is not further enhanced in these double mutants (Figure 4A).

Interestingly, *arl-13;ift-139* mutants have shorter cilia, while *arl-13;mks-2* mutants display cilia lengths comparable to single mutants (Figures 4B andS4A). Notably, we observed that the cilia misdirection phenotype in *arl-13* mutants is neither enhanced nor suppressed by the loss of other cilia length regulator genes, such as *nekl-4*, *dyf-5*, or *cdkl-1*, despite length changes in the double mutants. Together, these findings suggest that cilia elongation and JCE are independent processes.

Loss of the nephronophthisis2 (NPHP2/inversin) enhances cilia misdirection phenotype in *arl-13* mutants

Barr and her colleagues previously showed that combined deletion of nephronophthisis-associated *nphp-2*/inversin and *arl-13* exacerbated the ciliary phenotypes.[48] In the current study, we aimed to investigate whether *arl-13;nphp-2* double mutants

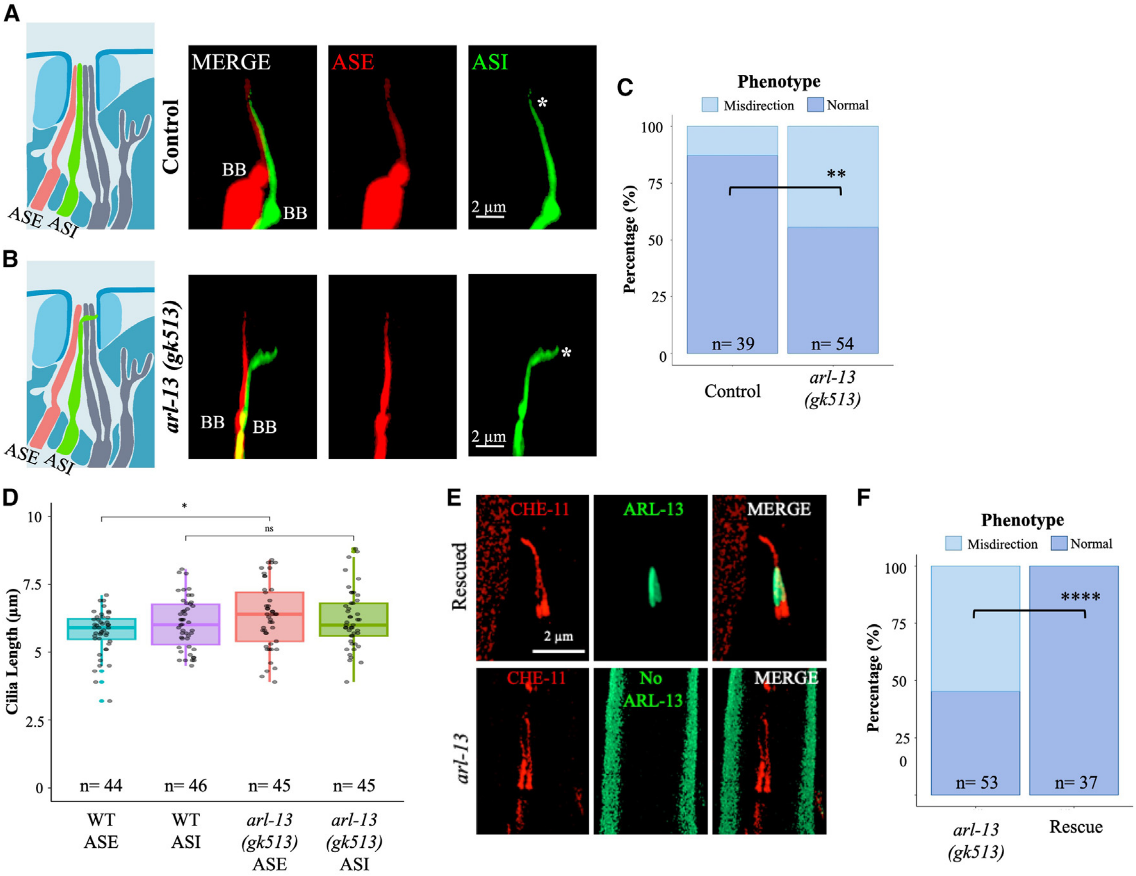

Figure 3. The juxtaposed cilia-cilia elongation (JCE) of ASE and ASI requires ARL-13

(A and B) The schematic displays the JCE of several cilia, including ASE (red) and ASI (green) in the head. Shown are images of fluorescent markers, *gcy-5::mCherry* for ASE and *str-3::gfp* for ASI cilia in wild-type and *arl-13* mutants. Scale bar: 2 µm.

(C) The normal and cilia misdirection phenotypes were categorized in wild-type and *arl-13(gk513)* single mutants and the percentage of counting was plotted. For statistical significance, Fisher's exact test was employed (**>0.01). The number of analyzed cilia for the wild type (*n*) and *arl-13(gk513)* (*n*) are 39 and 54, respectively.

(D) Shown are the cilia lengths of ASE and ASI sensory neurons in both wild-type and *arl-13* mutants along with the mean. *n* represents the number of cilia measured, while "ns" indicates no significant difference. *n* for WT ASE: 44, *n* for WT ASI: 46, *n* for *arl-13(gk513)* ASE: 45, *n* for *arl-13(gk513)* ASI: 45. The asterisk denotes statistical significance ($p < 0.05$).

(E) Shown are images of PHA and PHB cilia labeled with CHE-11::mCherry in *arl-13* mutants. The top images display the rescue of *arl-13* mutants using the ARL-13::GFP construct. Scale bar: 2 µm.

(F) Bar plot displaying the percentage of normal and misdirected phenotypes in *arl-13* mutants and *arl-13* rescued mutants. *n* represents the number of cilia analyzed (*n* for *arl-13 (gk513):* 53, *n* for rescue: 37).

would exhibit a more severe cilia misdirection phenotype. Consistent with expectation, simultaneous loss of *arl-13* and *nphp-2* results in the severe truncation of PHA and PHB cilia. The short cilia observed in *arl-13;nphp-2* double mutants (data not shown) make it difficult to definitively assess the presence of a cilia misdirection phenotype. The same work showed that the histone deacetylase 6 (*hdac-6*) restores the ciliary defect of *arl-13;nphp-2* double mutants, thus, we introduced the *hdac-6* mutants into the *arl-13;nphp-2* background. Interestingly, we observed a notable improvement in cilia length; however, the percentage of the cilia misdirection phenotype was dramatically increased in *arl-13;nphp-2;hdac-6* triple mutants compared to *arl-13;hdac-6* double mutants and *arl-13* single mutants (Figures S5A–S5C).

PHA and PHB cilia misdirection phenotype in *arl-13* mutants was not due to the BB mispositioning

Following that, we explore the underlying causes of PHA and PHB cilia misdirection in *arl-13* mutants. There are various potential explanations for the observed cilia misdirection phenotype. One possibility is that the shortening of PHA or PHB dendrites might result in the misplacement of the BB, from where the cilia emerge, thus cilia are disproportionately elongated. The previous work from our lab and other labs reported the mispositioning of BB in *mks-5(tm3100);nphp-4(tm925)* and *rpi-1(syb722);nphp-4(tm925)* double mutants[49,50] (Figure 5A).

To shed more light on these phenomena further, we determine the cilia misdirection phenotypes and (Figure 5B) measure cilia (Figure 5C) and dendrite lengths (Figure 5E), as well as the distance

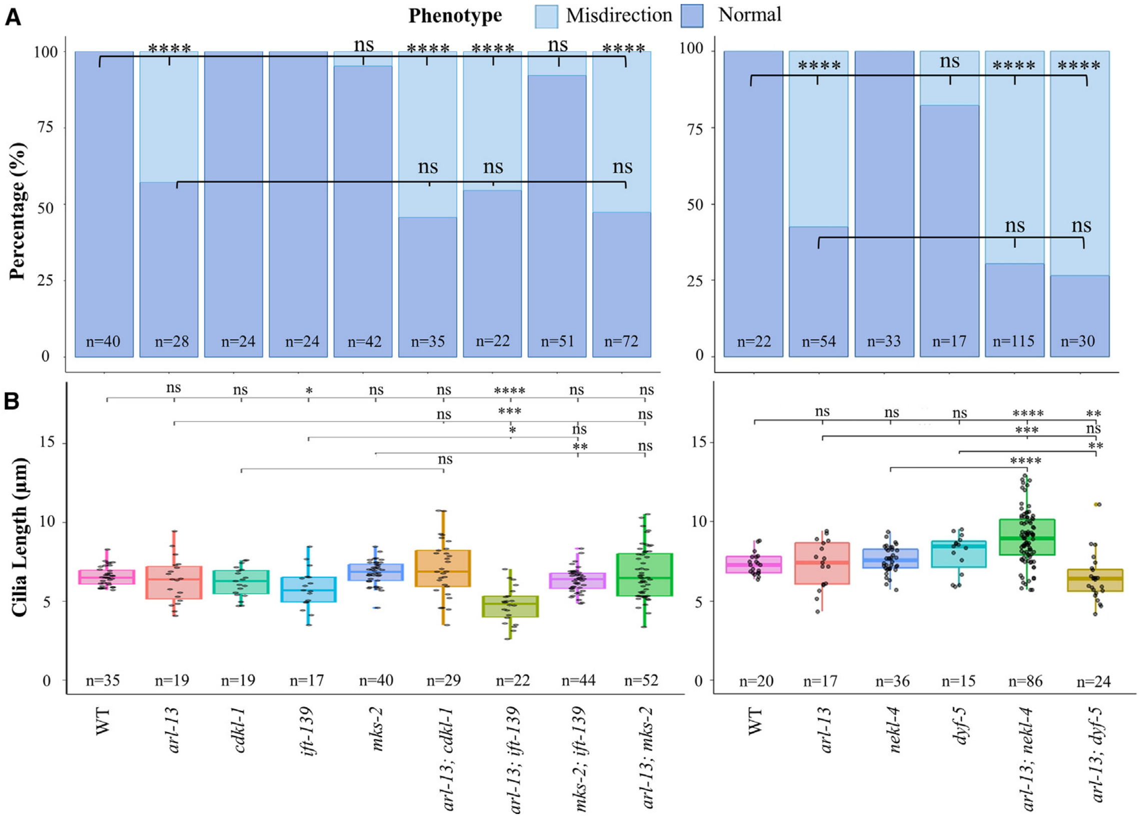

Figure 4. Cilia length and JCE are independent of each other

(A) Shown are the proportions of phenotypic distribution, categorizing normal and misdirection, in both wild-type and the specified mutants. Data were generated using either *srb-6promoter::gfp* (on the left side) or endogenously tagged IFT-74::GFP (on the right side). Fisher's exact statistical test was employed to compare wild-type vs. mutants and *arl-13* vs. double mutants (ns = not-significant, **** = 0.0001). *n* represents the number of cilia analyzed for each strain. Refer to the key resources table for more details.

(B) Shown are the bar plots displaying the lengths of PHA cilia for both wild-type and stated mutants along with the mean. Wilcoxon paired-two test is employed (ns = not-significant, * = 0.05, ** = 0.01, *** = 0.001, **** = 1e-04). *n* specifies the analyzed cilia number for each stain.

between the PHA and PHB BBs (Figure 5F) in several strains, including wild-type, *rpi-1(syb722)*, *nphp-4(tm925)*, *rpi-1(syb722);nphp-4(tm925)*, *mks-5(tm3100);nphp-4(tm925)*, and *arl-13(gk513).* Surprisingly, we discover that the PHA/PHB dendrite is shorter in mutants such as *mks-5(tm3100)*, *rpi-1(syb722)*, *nphp-4(tm925)*, and *arl-13(gk513)*, as well as double mutant combinations, than in the wild-type (Figure 5E). This reduction in dendrite length does not correlate with the cilia misdirection phenotype because the cilia misdirection phenotype is only statistically obvious in *arl-13(gk513)* single mutants, *rpi-1(syb722);nphp-4(tm925)* and *mks-5(tm3100);nphp-4(tm925)* double mutants.

However, we observe a significant difference in the distance between the PHA and PHB BBs in the double mutants *rpi-1;nphp-4* and *mks-5;nphp-4.* There may be a connection between BB positionings and the cilia misdirection phenotype for the double mutants, but not for the *arl-13(tm2322)* mutants, as this distance is not notably different between the *arl-13(gk513)* mutants and the wild-type (Figure 5F).

In *C. elegans*, the cilia located at the distal terminals of the dendrites are encircled by sheath glial cells. The loss of *arl-13* and *rpi-1* may potentially disturb the surrounding environment of cilia, resulting in abnormal JCE. To investigate this, mutants expressing *F16F9.3promoter::GFP* transcriptional fusion (generously provided by Dr. B K. Yoder, University of Alabama at Birmingham Medical Center) and translational OSM-3::mCherry were generated, enabling us to monitor both the sheath glial cells and cilia, respectively[33] (Figures S7A and S7B). Our findings indicate that the sheath glial cells remain unaffected in mutants, including *arl-13*, *rpi-1;nphp-4* double mutants, and their respective single mutants. Taken together, our findings provide valuable insights into the likely mechanisms underlying PHA and PHB cilia misdirection in *rpi-1;nphp-4* and *mks-5;nphp-4* double mutants. BB mispositioning may be the main factor causing the cilia misdirection phenotype in *rpi-1;nphp-4* and *mks-5;nphp-4* double mutants, but not in *arl-13* single mutants.

The BBSome component *bbs-8* rescues the cilia misdirection defect of *arl-13*

The observed cilia misdirection phenotype in *arl-13* mutants might be due to disruption in the ciliary membrane or cilia guidance. Similar to the axon outgrowth in neurons, the PHA and PHB cilia may require guidance signals to establish a precise

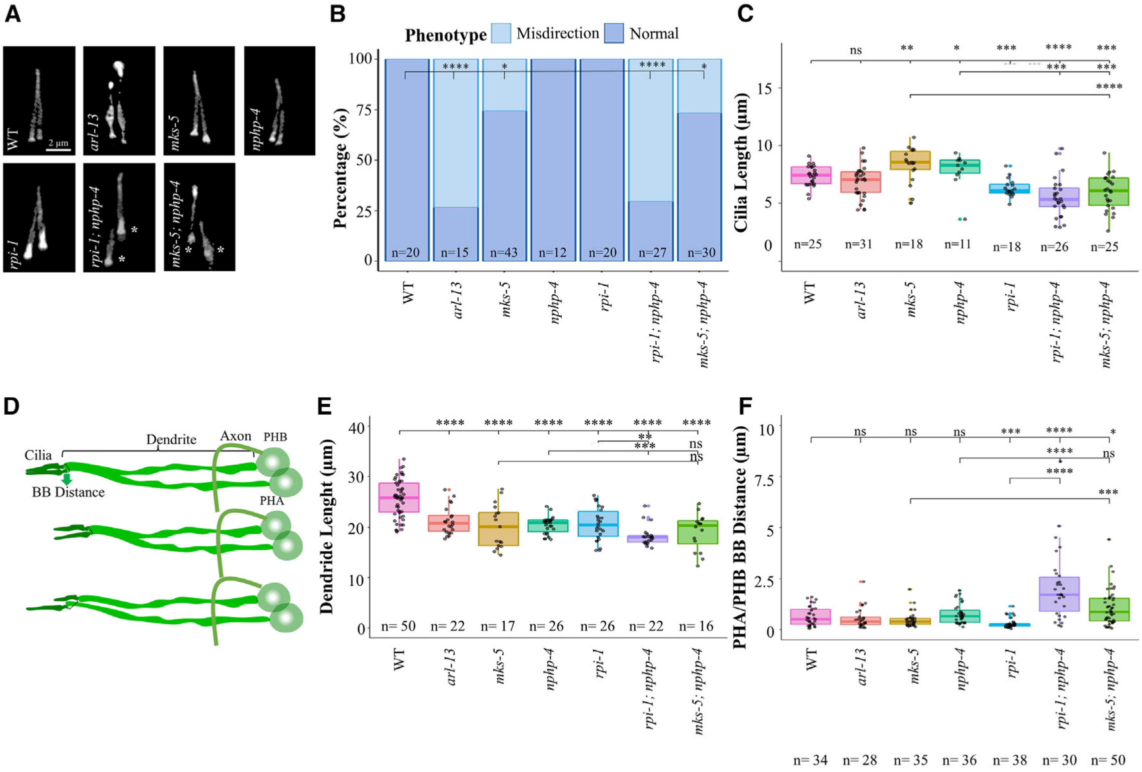

Figure 5. BB mispositioning accounts for the cilia misdirection phenotype of PHA and PHB cilia in *mks-5;nphp-4* and *rpi-1;nphp-4* double mutants, but in *arl-13* single mutants

(A) Shown are the representative confocal images displaying PHA and PHB cilia, marked with endogenous IFT-74::GFP fluorescent protein, from wild-type, *arl-13(gk513)*, *mks-5(tm3100)*, *nphp-4(tm925)*, *rpi-1(syb722)* single, *rpi-1(syb722);nphp-4(tm925)*, and *mks-5(tm3100);nphp-4(tm925)* double mutants. The asterisk (*) points to basal body positions of PHA and PHB. Scale bar: 2 μm.

(B) The graph shows the distribution of PHA and PHB cilia phenotype of wild-type and indicated mutants as normal and misdirected. Fisher's exact statistical test is utilized to compare normal and cilia misdirection phenotypes (ns = not-significant, ** = 0.01, **** = 0.0001). *n* represents the number of cilia analyzed for each strain.

(C, E, and F) The boxplots show PHA cilia length (C), dendrite length (E), and the basal body distance between PHA and PHB cilia along with the mean (F). Wilcoxon paired statistical test is used for comparisons (ns = not-significant, * = 0.05, ** = 0.01, *** = 0.001, **** = 1e-04). The cilia number used is shown in n for (B), (C), (E), and (F) analysis.

(D) The illustrations display the whole PHA and PHB sensory neurons, including the cell body, axon, dendrite, basal body (BB), and cilia. Various phenotypes are depicted, including BB mispositioning coupled with cilia misdirection, as well as cilia misdirection without BB mispositioning.

JCE. In the navigation of the axonal growth cone (GC) in neurons, the critical components of MTs of GC were regulated by guidance cues, growth factors, and cell adhesion molecules. MTs are also the fundamental structural cores of cilia (also known as axonemes) surrounded by the ciliary membrane. Unidentified cell adhesion molecules and guidance cues may contribute to the juxtaposed elongation of the PHA and PHB cilia.

To explore this, we first direct our attention to the role of tubulin genes, particularly *tbb-4* (β-tubulins), which are crucial for the construction and stability of MTs in the ciliary axoneme. In particular, a missense mutation in *tbb-4(sa127)* has been demonstrated to destabilize MTs.[51] Sengupta and her colleagues have shown that *tbb-4(sa127)* can restore the missing AWB branching in *dyf-18* mutants.[52] We thus aim to investigate whether increased MT stability can modulate the cilia misdirection phenotype in *arl-13* mutants. Our analysis revealed that despite *arl-13;tbb-4(sa127)* double mutants exhibiting a cilia length comparable to that of the *tbb-4(sa127)* single mutants, the percentage of the cilia misdirection phenotype in the double mutants was similar to that of the *arl-13* single mutant (Figures 6A, S6A, and S6B). This suggests that MT-destabilizing mutation in *tbb-4* does not impact the cilia misdirection phenotype in *arl-13* mutants.

We next investigated whether disrupting tubulin transport by removing core components of IFT machinery, such as *ift-81*, would show any impact on the cilia misdirection phenotype in *arl-13* mutants. It is already well established that IFT, along with diffusion, plays a critical role in delivering tubulin into cilia.[51,53,54] The core components of IFT-B, specifically IFT74 and IFT81, establish a tubulin-binding module that facilitates the delivery of tubulin.[55,56] We created the double mutants *arl-13(gk513);ift-81(tm2355)* and imaged them (Figure 6A). Although the cilia of the *arl-13(gk513);ift-81(tm2355)* double and *ift-81(tm2355)* single mutants are both slightly

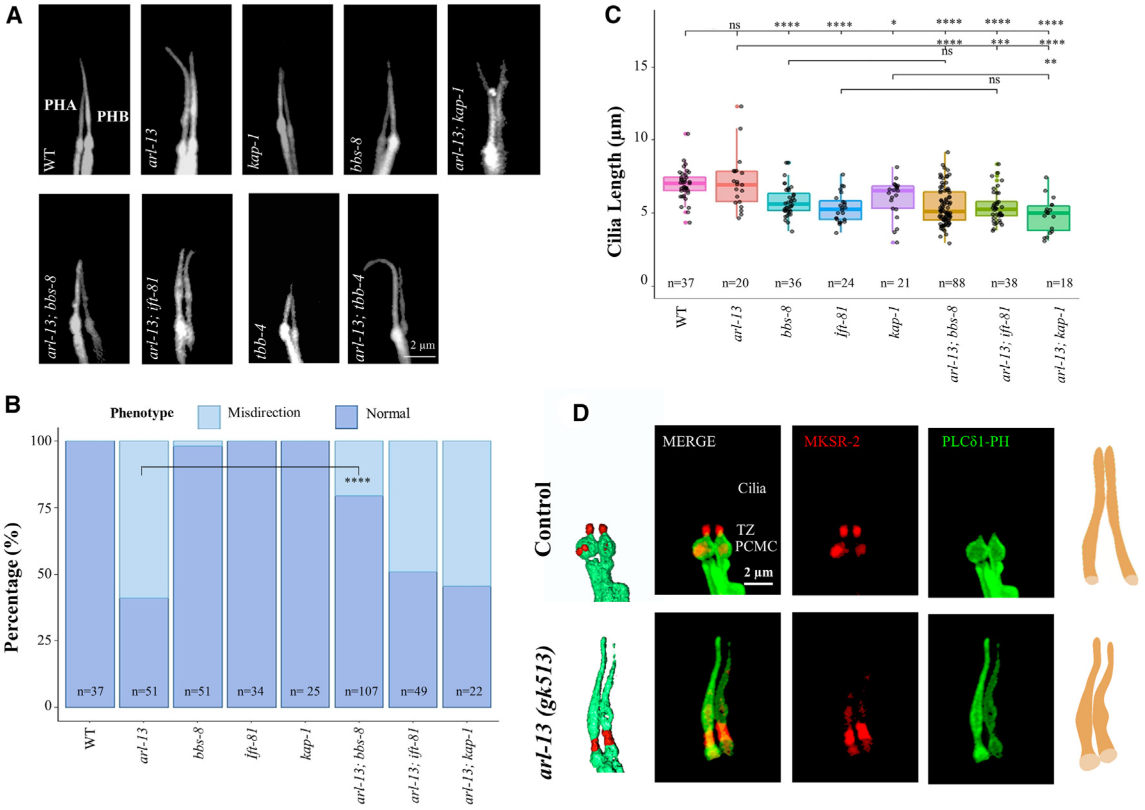

Figure 6. *bbs-8* partially rescues the cilia misdirection phenotype in the absence of *arl-13*

(A) The top image panel shows the PHA and PHB cilia, visualized with *srb-6::promoter::gfp* in the wild-type and indicated mutants. Scale bar: 2 µm.

(B) The stacked bar chart illustrates the percentage distribution of normal and misdirection phenotypic categories for PHA and PHB cilia. Fisher's exact test was applied for statistical analysis (ns = not significant, ** = 0.01, **** = 0.0001), with "ns" indicating non-significance. *n* represents the number of cilia analyzed for each strain.

(C) PHA cilia lengths are visualized in the graphic in wild-type and indicated mutants along with the mean. The Wilcoxon paired-two test is utilized for comparing the lengths of cilia (ns = not-significant, * = 0.05, ** = 0.01, *** = 0.001, **** = 1e−04).

The worm numbers used in (B) and (C) are shown in *n* for each strain.

(D) Shown are the distribution of GFP::PLCδ1-PH (and MKSR-2::tdTomato (a transition zone marker) in wild-type and *arl-13* mutants. The representative schematics are shown next to fluorescent images. Scale bar: 2 µm.

shorter than those of the wild-type, the percentage of cilia misdirection phenotype remains unaffected. This suggests that *arl-13(gk513);ift-81(tm2355)* double exhibit a similar percentage of PHA and PHB cilia misdirection to that of the *arl-13* single mutant (Figures 6B and 6C). Furthermore, the disruption of heterotrimeric kinesin II, the anterograde IFT kinesin, did not restore the cilia misdirection phenotype in *arl-13* mutants. Due to short cilia with *osm-3*, the homodimeric kinesin-2 for the anterograde IFT, we could not draw any conclusion with *osm-3;arl-13* double mutants about its effects on cilia misdirection phenotype.

The currently unidentified adhesion molecules may play a role in the joining of PHA and PHB cilia. The absence or mislocalization of as-yet-unidentified adhesion molecules may contribute to the cilia misdirection phenotype observed in PHA and PHB cilia in *arl-13* mutants. Ciliary membrane protein transport is in part mediated by IFT and BBSome complexes. BBSome travels together with IFT and requires the export of membrane proteins from cilia. We investigated whether the cilia misdirection phenotype in *arl-13* mutants could be modified by the impact of interrupting membrane transport by removing a component of the BBSome, namely *bbs-8*. We created *arl-13;bbs-8(nx77)* double mutants and determined the cilia length and cilia misdirection phenotypes. We found that the loss of BBSome partially suppressed the cilia misdirection phenotype in *arl-13* mutants. These results indicate that disruption of BBSome-mediated membrane transport can partially reduce the effects of *arl-13* mutants in PHA and PHB cilia. All these findings suggest changes in the contents of the ciliary membrane. To investigate this further, we examine alterations in the ciliary membrane of *arl-13* mutants. Under normal conditions, the ciliary membranes typically lack phosphatidylinositol 4,5-bisphosphate [PI(4,5)P2], as shown by the visualization of GFP::PLCδ1-PH. GFP:PLCδ1-PH decorates the PCMC and dendritic membrane, and is distinctly absent from the ciliary membranes in the wild-type[57–61] (Figure 6D). However, in *arl-13* mutants, GFP:PLCδ1-PH associates with the ciliary membrane, indicating noticeable changes in its ciliary membrane composition. Further molecular analyses on the ciliary membranes in *arl-13* mutants will provide a better understanding.

DISCUSSION

Here, we show that ARL-13/ARL13B regulates the coordinated elongation of juxtaposed cilia originating from distinct sensory neurons, likely by modulating the ciliary membrane in a BBSome-dependent manner.

A significant finding of our work is the independence of JCE from cilia length. While the molecular mechanism driving cilia length is well known, our data suggest that JCE occurs independently of cilia length. This decoupling is evidenced by the observation that in *arl-13* mutants, the lengths of misdirected cilia remain relatively unchanged compared to wild-type cilia. Moreover, the percentage of cilia misdirection phenotype observed in *arl-13* mutants does not change significantly, except for *arl-13;nphp-2;hdac-6 triple* mutants, regardless of whether cilia length is shortened or extended in various double mutants. This indicates that, while cilia length is influenced by a variety of genes, the coordination of joint cilia elongation is regulated by distinct pathways involving *ARL-13*.

Our results highlight the role of the BBSome in facilitating JCE. The partial rescue of the cilia misdirection phenotype in *arl-13* mutants by the absence of BBSome components suggests a functional interplay between these proteins. In contrast, *tbb-4(sa127);arl-13* double mutants exhibit a similar level of misdirection as *arl-13* single mutants, even though they have truncated cilia when shifted to 25°C. While the BBSome is an essential regulator of proteins in the ciliary membrane, ciliary singlet MT stability is reportedly enhanced by *tbb-4(sa127)* mutants carrying the L253F missense, thus suggesting the membrane modulation rather than the axoneme is crucial for the joint and side to side elongation of cilia.[47] Furthermore, our work revealed that ciliary membrane phospholipid compositions are altered in *arl-13* single mutants.

Our analysis indicates the importance of the distance between the BB of juxtaposed cilia for the proper formation of JCE. While dendrite shortening does not necessarily correlate with the cilia misdirection phenotype observed, BB mispositioning emerges as a critical factor in specific double mutants, such as *rpi-1;nphp-4,* and *mks-5;nphp-4*. However, it is unlikely that BB mispositioning serves as the primary driver of the cilia misdirection phenotype seen in *arl-13* mutants.

Instead, our findings suggest that BB mispositioning plays a significant role in joint cilia elongation, implicating TZ proteins, such as NPHP-4 and MKS-5, as well as ciliary proteins like RPI-1/DCDC2 in this process. The critical roles of these TZ proteins and ciliary proteins in regulating JCE are interesting, particularly considering their involvement in various ciliopathies, including Meckel syndrome, nephronophthisis (NPHP), and related disorders (NPHP-RC). Furthermore, the finding that ciliary misdirection is further enhanced in *arl-13, nphp-2/inversin*, and *hdac-6* mutants aligns with previous reports of a genetic interaction between these genes.[48] Nevertheless, our findings implicate *nphp-2/inversin* and potentially *hdac-6* in the JCE.

Sengupta and her colleagues employed ssTEM[15,19] that revealed the juxtaposition of cilia from distinct sensory neurons. However, the mechanism by which the juxtaposed cilia-cilia extensions (JCEs) are maintained remains unknown.[15,19] Our fluorescence-based visualization system has confirmed the JCE. Through analyzing across various ages of *C. elegans*, we observed that once established, the JCE persists over extended periods. The long-lasting nature of JCE suggests the likelihood of direct contact between the two ciliary membranes, with adhesion molecules potentially mediating stable cilia-cilia contact. Consistent with a suggestion, the adhesion molecules are involved in the cilia-cilia contact in mammals as the inhibitor for maturation of N-linked glycoproteins, swainsonine, was found to reduce the cilia-cilia contact between cells.[15] Similarly, the attachment of flagella to a surface in *C. reinhardtii* requires the presence of adhesion molecules. In the process of mating, *C. reinhardtii* employs flagellar adhesion molecules.[62]

Interestingly, several cell-cell adhesion molecules, including GPC5 (glypican-5), ITGA8 and Pcdh15a, ITGB1 (integrinβ1), and CD44 were reported to localize to cilia,[63–65] and further work is needed to explore their involvements in cilia-cilia contact. Although our work does not directly explore the specific mechanism governing cilia-cilia contact, it provides evidence supporting the critical involvement of ARL-13 and BBSome-related membrane activities in facilitating such contact. Our previous work revealed that ARL-13 is important for the delivery of membrane proteins to cilia,[42] maybe the delivery of unknown cell adhesion molecules cannot be made in the absence of ARL-13, thus this may result in defects in JCE. Furthermore, our current work provides evidence of changes in the ciliary membrane contents. The unique contributions of *arl-13* to the JCE warrant further exploration, providing a foundation for future investigations into the complex regulatory mechanisms governing cilia organization and function.

What causes the eight cilia (ASE, ASG, ASH, ASI, ASJ, ASK, ADF, and ADL) from distinct sensory neurons in the head to converge at a central point and extend in such close proximity? One possibility is that their joint elongation may be anatomically necessary due to their emergence into the same channel. However, this anatomical arrangement alone may not fully explain the close cilia-cilia contact, especially since similar contact occurs in mammals.[15,66]

This proximity may serve as a new way of communication between two cilia, similar to the recently discovered axo-ciliary synapses. The previous work has demonstrated neurotransmitters released by axons participate in axo-ciliary synapses, triggering specific signaling in the nucleus.[14] The unexpected connection between the primary cilium and the axon has not only opened up new avenues but has also increased the interest of the cilia community. Furthermore, cilia from various organisms, including mammals, *Chlamydomonas*, and *C. elegans*, release ciliary extracellular vehicles (EVs). Do EVs play a role in cilia-cilia contact? More work will uncover the mystery of the cilia-cilia connection.

Limitations of the study

The current work has a number of limitations even if it offers insightful data about the mechanisms of JCE. Firstly, it primarily concentrates on a select few genes, notably *ARL-13*, which might overlook other potentially significant genetic contributors to JCE. A wider genetic screen is necessary to figure out a more comprehensive network of genes involved in JCE. Second, while the data suggests that ARL13 plays a part in modulating the ciliary membrane, the precise molecular pathways are still unclear, suggesting that more in-depth molecular work is required to elucidate these interactions and pinpoint important membrane constituents, such as adhesion molecules. Another limitation is the use of fluorescence-based techniques to visualize cilia-cilia contact. While these methods are valuable for observing cellular structures, the available confocal microscopy lacks the high resolution needed for detailed analysis. The integration of focused ion beam scanning electron microscopy (FIB-SEM) could address this limitation by providing high-resolution imaging, enabling a more precise and unbiased examination of cilia-cilia contact and interactions.

RESOURCE AVAILABILITY

Lead contact

Further information and requests for resources and reagents should be directed to and will be fulfilled by the lead contact, Oktay I. Kaplan (oktay.kaplan@agu.edu.tr).

Materials availability

Generated *C. elegans* strains and used plasmid for this study are available from the lead contact (oktay.kaplan@agu.edu.tr) upon request. The key resources table lists identifiers for all the shared resources.

Data and code availability

Data for PHA and PHA and ASE and ASI cilia length measurements and classified cilia phenotypes are publicly available at Zenodo (https://doi.org/10.5281/zenodo.14589265).

Codes used for generating plot plots with statistical analysis for this study are publicly available at Zenodo (https://doi.org/10.5281/zenodo.14589265) and GitHub (https://github.com/mervegulturan/ARL13B-regulates-Juxtaposed-Cilia-Cilia-Elongation-in-BBSome-dependent-manner-in-C-elegans) repositories. Their specific URL's and DOIs are available in the key resources table as of the date of publication.

Any additional information required to reanalyze the data reported in this paper is available from the lead contact upon request.

ACKNOWLEDGMENTS

We thank Ferhan Yenisert for her assistance in creating a transgenic strain and Bradley K. Yoder for supplying the plasmid (*F16F9.3*promoter::GFP, PCP41). Several strains were acquired from the CGC, which is supported by the NIH Office of Research Infrastructure Programs (P40 OD010440), United States. This research was supported by the Health Institutes of Turkey (TÜSEB) (Project number: 28555), Türkiye to S.C.

AUTHOR CONTRIBUTIONS

Conceptualization, M.G.T., S.C., and O.I.K.; methodology, O.I.K., M.G.T., S.C., and H.K.; formal analysis, M.G.T.; investigation, M.G.T. and S.C.; writing – original draft, S.C., M.G.T., and O.I.K.; writing – review & editing, S.C., M.G.T., H.K., and O.I.K.; visualization, S.C. and M.G.T.; funding acquisition, S.C.; resources, O.I.K. and S.C.; supervision, O.I.K. and S.C.

DECLARATION OF INTERESTS

The authors declare no competing interests.

STAR★METHODS

Detailed methods are provided in the online version of this paper and include the following:

- KEY RESOURCES TABLE
- EXPERIMENTAL MODEL AND STUDY PARTICIPANT DETAILS
- METHOD DETAILS
    - CRISPR/*Cas9* in *C. elegans* and microinjection
    - Confocal microscopy imaging and analysis process
    - Dendrite length measurements
    - Stage analysis
- QUANTIFICATION AND STATISTICAL ANALYSIS

SUPPLEMENTAL INFORMATION

Supplemental information can be found online at https://doi.org/10.1016/j.isci.2025.111791.

Received: February 2, 2024
Revised: August 30, 2024
Accepted: January 8, 2025
Published: January 10, 2025

REFERENCES

1. Garcia, G., Raleigh, D.R., and Reiter, J.F. (2018). How the Ciliary Membrane Is Organized Inside-Out to Communicate Outside-In. Curr. Biol. *28*, R421–R434. https://doi.org/10.1016/j.cub.2018.03.010.
2. Wang, S., Burton, J.C., Behringer, R.R., and Larina, I.V. (2015). In vivo micro-scale tomography of ciliary behavior in the mammalian oviduct. Sci. Rep. *5*, 13216. https://doi.org/10.1038/srep13216.
3. Warrington, T.B. (2018). Computational and molecular dissection of an X-box cis-Regulatory module. Preprint at arXiv. https://doi.org/10.48550/ARXIV.1810.00478.
4. Greenan, G.A., Vale, R.D., and Agard, D.A. (2020). Electron cryotomography of intact motile cilia defines the basal body to axoneme transition. J. Cell Biol. *219*, e201907060. https://doi.org/10.1083/jcb.201907060.
5. Jenkins, P.M., McEwen, D.P., and Martens, J.R. (2009). Olfactory Cilia: Linking Sensory Cilia Function and Human Disease. Chem. Senses *34*, 451–464. https://doi.org/10.1093/chemse/bjp020.
6. Berbari, N.F., O'Connor, A.K., Haycraft, C.J., and Yoder, B.K. (2009). The Primary Cilium as a Complex Signaling Center. Curr. Biol. *19*, R526–R535. https://doi.org/10.1016/j.cub.2009.05.025.
7. Ji, W., Tang, Z., Chen, Y., Wang, C., Tan, C., Liao, J., Tong, L., and Xiao, G. (2022). Ependymal Cilia: Physiology and Role in Hydrocephalus. Front. Mol. Neurosci. *15*, 927479. https://doi.org/10.3389/fnmol.2022.927479.
8. Kozminski, K.G., Johnson, K.A., Forscher, P., and Rosenbaum, J.L. (1993). A motility in the eukaryotic flagellum unrelated to flagellar beating. Proc. Natl. Acad. Sci. USA *90*, 5519–5523. https://doi.org/10.1073/pnas.90.12.5519.
9. Cao, Y., Park, A., and Sun, Z. (2010). Intraflagellar Transport Proteins Are Essential for Cilia Formation and for Planar Cell Polarity. J. Am. Soc. Nephrol. *21*, 1326–1333. https://doi.org/10.1681/ASN.2009091001.
10. Eguether, T., San Agustin, J.T., Keady, B.T., Jonassen, J.A., Liang, Y., Francis, R., Tobita, K., Johnson, C.A., Abdelhamed, Z.A., Lo, C.W., and Pazour, G.J. (2014). IFT27 Links the BBSome to IFT for Maintenance of the Ciliary Signaling Compartment. Dev. Cell *31*, 279–290. https://doi.org/10.1016/j.devcel.2014.09.011.
11. Singh, S.K., Gui, M., Koh, F., Yip, M.C., and Brown, A. (2020). Structure and activation mechanism of the BBSome membrane protein trafficking complex. Elife *9*, e53322. https://doi.org/10.7554/eLife.53322.

12. Nozaki, S., Castro Araya, R.F., Katoh, Y., and Nakayama, K. (2019). Requirement of IFT-B–BBSome complex interaction in export of GPR161 from cilia. Biol. Open *8*, bio043786. https://doi.org/10.1242/bio.043786.

13. Liew, G.M., Ye, F., Nager, A.R., Murphy, J.P., Lee, J.S., Aguiar, M., Breslow, D.K., Gygi, S.P., and Nachury, M.V. (2014). The Intraflagellar Transport Protein IFT27 Promotes BBSome Exit from Cilia through the GTPase ARL6/BBS3. Dev. Cell *31*, 265–278. https://doi.org/10.1016/j.devcel.2014.09.004.

14. Sheu, S.-H., Upadhyayula, S., Dupuy, V., Pang, S., Deng, F., Wan, J., Walpita, D., Pasolli, H.A., Houser, J., Sanchez-Martinez, S., et al. (2022). A serotonergic axon-cilium synapse drives nuclear signaling to alter chromatin accessibility. Cell *185*, 3390–3407.e18. https://doi.org/10.1016/j.cell.2022.07.026.

15. Ott, C., Elia, N., Jeong, S.Y., Insinna, C., Sengupta, P., and Lippincott-Schwartz, J. (2012). Primary cilia utilize glycoprotein-dependent adhesion mechanisms to stabilize long-lasting cilia-cilia contacts. Cilia *1*, 3. https://doi.org/10.1186/2046-2530-1-3.

16. Ward, S., Thomson, N., White, J.G., and Brenner, S. (1975). Electron microscopical reconstruction of the anterior sensory anatomy of the nematode caenorhabditis elegans. J. Comp. Neurol. *160*, 313–337. https://doi.org/10.1002/cne.901600305.

17. Ware, R.W., Clark, D., Crossland, K., and Russell, R.L. (1975). The nerve ring of the nematode Caenorhabditis elegans : Sensory input and motor output. J. Comp. Neurol. *162*, 71–110. https://doi.org/10.1002/cne.901620106.

18. Perkins, L.A., Hedgecock, E.M., Thomson, J.N., and Culotti, J.G. (1986). Mutant sensory cilia in the nematode Caenorhabditis elegans. Dev. Biol. *117*, 456–487. https://doi.org/10.1016/0012-1606(86)90314-3.

19. Doroquez, D.B., Berciu, C., Anderson, J.R., Sengupta, P., and Nicastro, D. (2014). A high-resolution morphological and ultrastructural map of anterior sensory cilia and glia in Caenorhabditis elegans. Elife *3*, e01948. https://doi.org/10.7554/eLife.01948.

20. Kaplan, O.I., Doroquez, D.B., Cevik, S., Bowie, R.V., Clarke, L., Sanders, A.A.W.M., Kida, K., Rappoport, J.Z., Sengupta, P., and Blacque, O.E. (2012). Endocytosis Genes Facilitate Protein and Membrane Transport in C. elegans Sensory Cilia. Curr. Biol. *22*, 451–460. https://doi.org/10.1016/j.cub.2012.01.060.

21. Satish Tammana, T.V., Tammana, D., Diener, D.R., and Rosenbaum, J. (2013). Centrosomal protein CEP104/Chlamydomonas FAP256 moves to the ciliary tip during cilia assembly. J. Cell Sci. *126*, jcs.133439. https://doi.org/10.1242/jcs.133439.

22. Park, K., Li, C., Tsiropoulou, S., Gonçalves, J., Kondratev, C., Pelletier, L., Blacque, O.E., and Leroux, M.R. (2021). CDKL kinase regulates the length of the ciliary proximal segment. Curr. Biol. *31*, 2359–2373.e7. https://doi.org/10.1016/j.cub.2021.03.068.

23. Shi, P., Hoang-Minh, L.B., Tian, J., Cheng, A., Basrai, R., Kalaria, N., Lebowitz, J.J., Khoshbouei, H., Deleyrolle, L.P., and Sarkisian, M.R. (2021). HDAC6 Signaling at Primary Cilia Promotes Proliferation and Restricts Differentiation of Glioma Cells. Cancers *13*, 1644. https://doi.org/10.3390/cancers13071644.

24. Otto, E.A., Schermer, B., Obara, T., O'Toole, J.F., Hiller, K.S., Mueller, A.M., Ruf, R.G., Hoefele, J., Beekmann, F., Landau, D., et al. (2003). Mutations in INVS encoding inversin cause nephronophthisis type 2, linking renal cystic disease to the function of primary cilia and left-right axis determination. Nat. Genet. *34*, 413–420. https://doi.org/10.1038/ng1217.

25. Chaya, T., Omori, Y., Kuwahara, R., and Furukawa, T. (2014). ICK is essential for cell type-specific ciliogenesis and the regulation of ciliary transport. EMBO J. *33*, 1227–1242. https://doi.org/10.1002/embj.201488175.

26. Sergouniotis, P.I., Chakarova, C., Murphy, C., Becker, M., Lenassi, E., Arno, G., Lek, M., MacArthur, D.G., UCL-Exomes Consortium, Bhattacharya, S.S., et al. (2014). Biallelic Variants in TTLL5, Encoding a Tubulin Glutamylase, Cause Retinal Dystrophy. Am. J. Hum. Genet. *94*, 760–769. https://doi.org/10.1016/j.ajhg.2014.04.003.

27. Prasai, A., Schmidt Cernohorska, M., Ruppova, K., Niederlova, V., Andelova, M., Draber, P., Stepanek, O., and Huranova, M. (2020). The BBSome assembly is spatially controlled by BBS1 and BBS4 in human cells. J. Biol. Chem. *295*, 14279–14290. https://doi.org/10.1074/jbc.RA120.013905.

28. Li, J.B., Gerdes, J.M., Haycraft, C.J., Fan, Y., Teslovich, T.M., May-Simera, H., Li, H., Blacque, O.E., Li, L., Leitch, C.C., et al. (2004). Comparative Genomics Identifies a Flagellar and Basal Body Proteome that Includes the BBS5 Human Disease Gene. Cell *117*, 541–552. https://doi.org/10.1016/S0092-8674(04)00450-7.

29. Blacque, O.E., Reardon, M.J., Li, C., McCarthy, J., Mahjoub, M.R., Ansley, S.J., Badano, J.L., Mah, A.K., Beales, P.L., Davidson, W.S., et al. (2004). Loss of C. elegans BBS-7 and BBS-8 protein function results in cilia defects and compromised intraflagellar transport. Genes Dev. *18*, 1630–1642. https://doi.org/10.1101/gad.1194004.

30. Girard, M., Bizet, A.A., Lachaux, A., Gonzales, E., Filhol, E., Collardeau-Frachon, S., Jeanpierre, C., Henry, C., Fabre, M., Viremouneix, L., et al. (2016). DCDC2 Mutations Cause Neonatal Sclerosing Cholangitis: HUMAN MUTATION. Hum. Mutat. *37*, 1025–1029. https://doi.org/10.1002/humu.23031.

31. Valente, E.M., Logan, C.V., Mougou-Zerelli, S., Lee, J.H., Silhavy, J.L., Brancati, F., Iannicelli, M., Travaglini, L., Romani, S., Illi, B., et al. (2010). Mutations in TMEM216 perturb ciliogenesis and cause Joubert, Meckel and related syndromes. Nat. Genet. *42*, 619–625. https://doi.org/10.1038/ng.594.

32. Sang, L., Miller, J.J., Corbit, K.C., Giles, R.H., Brauer, M.J., Otto, E.A., Baye, L.M., Wen, X., Scales, S.J., Kwong, M., et al. (2011). Mapping the NPHP-JBTS-MKS Protein Network Reveals Ciliopathy Disease Genes and Pathways. Cell *145*, 513–528. https://doi.org/10.1016/j.cell.2011.04.019.

33. Williams, C.L., Winkelbauer, M.E., Schafer, J.C., Michaud, E.J., and Yoder, B.K. (2008). Functional Redundancy of the B9 Proteins and Nephrocystins in Caenorhabditis elegans Ciliogenesis. Mol. Biol. Cell *19*, 2154–2168. https://doi.org/10.1091/mbc.e07-10-1070.

34. Shu, X., Fry, A.M., Tulloch, B., Manson, F.D.C., Crabb, J.W., Khanna, H., Faragher, A.J., Lennon, A., He, S., Trojan, P., et al. (2005). RPGR ORF15 isoform co-localizes with RPGRIP1 at centrioles and basal bodies and interacts with nucleophosmin. Hum. Mol. Genet. *14*, 1183–1197. https://doi.org/10.1093/hmg/ddi129.

35. Gorden, N.T., Arts, H.H., Parisi, M.A., Coene, K.L.M., Letteboer, S.J.F., van Beersum, S.E.C., Mans, D.A., Hikida, A., Eckert, M., Knutzen, D., et al. (2008). CC2D2A Is Mutated in Joubert Syndrome and Interacts with the Ciliopathy-Associated Basal Body Protein CEP290. Am. J. Hum. Genet. *83*, 559–571. https://doi.org/10.1016/j.ajhg.2008.10.002.

36. Rachel, R.A., Yamamoto, E.A., Dewanjee, M.K., May-Simera, H.L., Sergeev, Y.V., Hackett, A.N., Pohida, K., Munasinghe, J., Gotoh, N., Wickstead, B., et al. (2015). CEP290 alleles in mice disrupt tissue-specific cilia biogenesis and recapitulate features of syndromic ciliopathies. Hum. Mol. Genet. *24*, 3775–3791. https://doi.org/10.1093/hmg/ddv123.

37. Canning, P., Park, K., Gonçalves, J., Li, C., Howard, C.J., Sharpe, T.D., Holt, L.J., Pelletier, L., Bullock, A.N., and Leroux, M.R. (2018). CDKL Family Kinases Have Evolved Distinct Structural Features and Ciliary Function. Cell Rep. *22*, 885–894. https://doi.org/10.1016/j.celrep.2017.12.083.

38. Cevik, S., Peng, X., Beyer, T., Pir, M.S., Yenisert, F., Woerz, F., Hoffmann, F., Altunkaynak, B., Pir, B., Boldt, K., et al. (2023). WDR31 displays functional redundancy with GTPase-activating proteins (GAPs) ELMOD and RP2 in regulating IFT complex and recruiting the BBSome to cilium. Life Sci. Alliance *6*, e202201844. https://doi.org/10.26508/lsa.202201844.

39. O'Hagan, R., Silva, M., Nguyen, K.C.Q., Zhang, W., Bellotti, S., Ramadan, Y.H., Hall, D.H., and Barr, M.M. (2017). Glutamylation Regulates Transport, Specializes Function, and Sculpts the Structure of Cilia. Curr. Biol. *27*, 3430–3441.e6. https://doi.org/10.1016/j.cub.2017.09.066.

40. Power, K.M., Nguyen, K.C., Silva, A., Singh, S., Hall, D.H., Rongo, C., and Barr, M.M. (2024). NEKL-4 regulates microtubule stability and mitochondrial health in C. elegans ciliated neurons. Preprint at bioRxiv. https://doi.org/10.1101/2024.02.14.580304.

41. Power, K.M., Akella, J.S., Gu, A., Walsh, J.D., Bellotti, S., Morash, M., Zhang, W., Ramadan, Y.H., Ross, N., Golden, A., et al. (2020). Mutation of NEKL-4/NEK10 and TTLL genes suppress neuronal ciliary degeneration caused by loss of CCPP-1 deglutamylase function. PLoS Genet. *16*, e1009052. https://doi.org/10.1371/journal.pgen.1009052.

42. Cevik, S., Hori, Y., Kaplan, O.I., Kida, K., Toivenon, T., Foley-Fisher, C., Cottell, D., Katada, T., Kontani, K., and Blacque, O.E. (2010). Joubert syndrome Arl13b functions at ciliary membranes and stabilizes protein transport in Caenorhabditis elegans. J. Cell Biol. *188*, 953–969. https://doi.org/10.1083/jcb.200908133.

43. Pir, M.S., Begar, E., Yenisert, F., Demirci, H.C., Korkmaz, M.E., Karaman, A., Tsiropoulou, S., Firat-Karalar, E.N., Blacque, O.E., Oner, S.S., et al. (2024). CilioGenics: an integrated method and database for predicting novel ciliary genes. Nucleic Acids Res. *52*, 8127–8145. https://doi.org/10.1093/nar/gkae554.

44. Hu, Z., Liang, Y., He, W., and Pan, J. (2015). Cilia Disassembly with Two Distinct Phases of Regulation. Cell Rep. *10*, 1803–1810. https://doi.org/10.1016/j.celrep.2015.02.044.

45. Tam, L.-W., Ranum, P.T., and Lefebvre, P.A. (2013). CDKL5 regulates flagellar length and localizes to the base of the flagella in Chlamydomonas. Mol. Biol. Cell *24*, 588–600. https://doi.org/10.1091/mbc.e12-10-0718.

46. Yi, P., Xie, C., and Ou, G. (2018). The kinases male germ cell-associated kinase and cell cycle-related kinase regulate kinesin-2 motility in Caenorhabditis elegans neuronal cilia. Traffic *19*, 522–535. https://doi.org/10.1111/tra.12572.

47. Scheidel, N., and Blacque, O.E. (2018). Intraflagellar Transport Complex A Genes Differentially Regulate Cilium Formation and Transition Zone Gating. Curr. Biol. *28*, 3279–3287.e2. https://doi.org/10.1016/j.cub.2018.08.017.

48. Warburton-Pitt, S.R.F., Silva, M., Nguyen, K.C.Q., Hall, D.H., and Barr, M.M. (2014). The nphp-2 and arl-13 Genetic Modules Interact to Regulate Ciliogenesis and Ciliary Microtubule Patterning in C. elegans. PLoS Genet. *10*, e1004866. https://doi.org/10.1371/journal.pgen.1004866.

49. Kaplan, O.İ. (2023). RPI-1 (human DCDC2) displays functional redundancy with Nephronophthisis 4 in regulating cilia biogenesis in C. elegans. Turk. J. Biol. *47*, 74–83. https://doi.org/10.55730/1300-0152.2642.

50. Williams, C.L., Masyukova, S.V., and Yoder, B.K. (2010). Normal Ciliogenesis Requires Synergy between the Cystic Kidney Disease Genes MKS-3 and NPHP-4. J. Am. Soc. Nephrol. *21*, 782–793. https://doi.org/10.1681/ASN.2009060597.

51. Hao, L., Thein, M., Brust-Mascher, I., Civelekoglu-Scholey, G., Lu, Y., Acar, S., Prevo, B., Shaham, S., and Scholey, J.M. (2011). Intraflagellar transport delivers tubulin isotypes to sensory cilium middle and distal segments. Nat. Cell Biol. *13*, 790–798. https://doi.org/10.1038/ncb2268.

52. Maurya, A.K., Rogers, T., and Sengupta, P. (2019). A CCRK and a MAK Kinase Modulate Cilia Branching and Length via Regulation of Axonemal Microtubule Dynamics in Caenorhabditis elegans. Curr. Biol. *29*, 1286–1300.e4. https://doi.org/10.1016/j.cub.2019.02.062.

53. Craft, J.M., Harris, J.A., Hyman, S., Kner, P., and Lechtreck, K.F. (2015). Tubulin transport by IFT is upregulated during ciliary growth by a cilium-autonomous mechanism. J. Cell Biol. *208*, 223–237. https://doi.org/10.1083/jcb.201409036.

54. Harris, J.A., Van De Weghe, J.C., Kubo, T., Witman, G.B., and Lechtreck, K.F. (2018). Diffusion rather than IFT provides most of the tubulin required for axonemal assembly. Preprint at bioRxiv. https://doi.org/10.1101/268573.

55. Kubo, T., Brown, J.M., Bellve, K., Craige, B., Craft, J.M., Fogarty, K., Lechtreck, K.F., and Witman, G.B. (2016). The IFT81 and IFT74 N-termini together form the major module for intraflagellar transport of tubulin. J. Cell Sci. jcs.187120. https://doi.org/10.1242/jcs.187120.

56. Bhogaraju, S., Cajanek, L., Fort, C., Blisnick, T., Weber, K., Taschner, M., Mizuno, N., Lamla, S., Bastin, P., Nigg, E.A., and Lorentzen, E. (2013). Molecular Basis of Tubulin Transport Within the Cilium by IFT74 and IFT81. Science *341*, 1009–1012. https://doi.org/10.1126/science.1240985.

57. DiTirro, D., Philbrook, A., Rubino, K., and Sengupta, P. (2019). The Caenorhabditis elegans Tubby homolog dynamically modulates olfactory cilia membrane morphogenesis and phospholipid composition. Elife *8*, e48789. https://doi.org/10.7554/eLife.48789.

58. Jensen, V.L., Li, C., Bowie, R.V., Clarke, L., Mohan, S., Blacque, O.E., and Leroux, M.R. (2015). Formation of the transition zone by Mks5/Rpgrip1L establishes a ciliary zone of exclusion (CIZE) that compartmentalises ciliary signalling proteins and controls PIP $_2$ ciliary abundance. EMBO J. *34*, 2537–2556. https://doi.org/10.15252/embj.201488044.

59. Qiu, H., Fujisawa, S., Nozaki, S., Katoh, Y., and Nakayama, K. (2021). Interaction of INPP5E with ARL13B is essential for its ciliary membrane retention but dispensable for its ciliary entry. Biol. Open *10*, bio.057653. https://doi.org/10.1242/bio.057653.

60. Fujisawa, S., Qiu, H., Nozaki, S., Chiba, S., Katoh, Y., and Nakayama, K. (2021). ARL3 and ARL13B GTPases participate in distinct steps of INPP5E targeting to the ciliary membrane. Biol. Open *10*, bio058843. https://doi.org/10.1242/bio.058843.

61. Humbert, M.C., Weihbrecht, K., Searby, C.C., Li, Y., Pope, R.M., Sheffield, V.C., and Seo, S. (2012). ARL13B, PDE6D, and CEP164 form a functional network for INPP5E ciliary targeting. Proc. Natl. Acad. Sci. USA *109*, 19691–19696. https://doi.org/10.1073/pnas.1210916109.

62. Xu, N., Oltmanns, A., Zhao, L., Girot, A., Karimi, M., Hoepfner, L., Kelterborn, S., Scholz, M., Beißel, J., Hegemann, P., et al. (2020). Altered N-glycan composition impacts flagella-mediated adhesion in Chlamydomonas reinhardtii. Elife *9*, e58805. https://doi.org/10.7554/eLife.58805.

63. Lee, M.N., Song, J.H., Oh, S.H., Tham, N.T., Kim, J.W., Yang, J.W., Kim, E.S., and Koh, J.T. (2020). The primary cilium directs osteopontin-induced migration of mesenchymal stem cells by regulating CD44 signaling and Cdc42 activation. Stem Cell Res. *45*, 101799. https://doi.org/10.1016/j.scr.2020.101799.

64. Goodman, L., and Zallocchi, M. (2017). Coordinate roles for Itgα8 and Pcdh15 in the regulation of cilia biogenesis in sensory cells. J. Cell Sci. *130*, jcs.206201. https://doi.org/10.1242/jcs.206201.

65. Li, F., Shi, W., Capurro, M., and Filmus, J. (2011). Glypican-5 stimulates rhabdomyosarcoma cell proliferation by activating Hedgehog signaling. J. Cell Biol. *192*, 691–704. https://doi.org/10.1083/jcb.201008087.

66. Ferkey, D.M., Sengupta, P., and L'Etoile, N.D. (2021). Chemosensory signal transduction in Caenorhabditis elegans. Genetics *217*, iyab004. https://doi.org/10.1093/genetics/iyab004.

67. Schindelin, J., Arganda-Carreras, I., Frise, E., Kaynig, V., Longair, M., Pietzsch, T., Preibisch, S., Rueden, C., Saalfeld, S., Schmid, B., et al. (2012). Fiji: an open-source platform for biological-image analysis. Nat. Methods *9*, 676–682. https://doi.org/10.1038/nmeth.2019.

68. Labun, K., Montague, T.G., Krause, M., Torres Cleuren, Y.N., Tjeldnes, H., and Valen, E. (2019). CHOPCHOP v3: expanding the CRISPR web toolbox beyond genome editing. Nucleic Acids Res. *47*, W171–W174. https://doi.org/10.1093/nar/gkz365.

69. Concordet, J.-P., and Haeussler, M. (2018). CRISPOR: intuitive guide selection for CRISPR/Cas9 genome editing experiments and screens. Nucleic Acids Res. *46*, W242–W245. https://doi.org/10.1093/nar/gky354.

70. Dickinson, D.J., Ward, J.D., Reiner, D.J., and Goldstein, B. (2013). Engineering the Caenorhabditis elegans genome using Cas9-triggered homologous recombination. Nat. Methods *10*, 1028–1034. https://doi.org/10.1038/nmeth.2641.

71. R Development Core Team (2010). R a Language and Environment for Statistical Computing: Reference Index (Vienna: R Foundation for Statistical Computing).

72. (2023). rstatix: Pipe-Friendly Framework for Basic Statistical Tests. https://cran.r-project.org/web/packages/rstatix/index.html.

73. Wickham, H. (2009). ggplot2: Elegant Graphics for Data Analysis (New York, NY: Springer New York). https://doi.org/10.1007/978-0-387-98141-3.

STAR★METHODS

KEY RESOURCES TABLE

REAGENT or RESOURCE	SOURCE	IDENTIFIER
Bacterial and virus strains		
Escherichia coli OP50	*Caenorhabditis* Genetics Center (CGC)	N/A
Chemicals, peptides, and recombinant proteins		
Levamisole Hydrochloride	ChemCruz, Santa Cruz Biotechnology, Inc.	sc-205730, 5 g
Halocarbon Oil	Sigma-Aldrich	9002-83-9
Immersion Oil	Sigma-Aldrich	56822-50 mL
Deposited data		
Codes used for creating plots and statistical analysis	This paper	https://github.com/mervegulturan/ARL13B-regulates-Juxtaposed-Cilia-Cilia-Elongation-in-BBSome-dependent-manner-in-C-elegans
Cilia-related measurements and phenotype classifications	This paper	https://doi.org/10.5281/zenodo.14589265
Experimental models: Organisms/strains		
Bristol wild-type	CGC	N2
bbs-5(gk537)	CGC	VC1316
bbs-7(ok1351)	CGC	RB1268
hdac-6(ok3203)	This paper	OIK150
mksr-1(tm3083)	Mitani Lab	FX03083
mks-2(nx111)	Blacque Lab	MX1251
mks-5(tm3100)	Blacque Lab	FX3100
mks-6(gk674)	Blacque Lab	VC1466
dyf-5(ok1177)	CGC	RB1148
nphp-2(gk653)	CGC	VC1428
nphp-4(tm925)	CGC	PT709
kap-1(ok676)	CGC	RB849
klp-13(tm3737)	Mitani Lab	
rpi-1(syb722)	Kaplan Lab	PHX722
nekl-4(tm4910)	Mitani Lab	FX04910
elmd-1(syb630)	Kaplan Lab	PHX630
ift-81(tm2355)	CGC	FX2355
ift-139(gk508)	CGC	VC1130
osm-3(p802)	CGC	PR802
bbs-8(nx77)	Blacque Lab	MX52
cdkl-1(ok2694)	CGC	RB2036
cep-104(tur012)	This work	OIK962
ccep-290(tm4927)	Dammermann Lab	DAM297
ttll-4(tm3310)	Yoshi	YT600
ttll-11(gk482)	CGC	VC1105
wdr-31(tm10423)	Kaplan Lab	OIK466
wdr-54(syb1005)	Kaplan Lab	PHX1005
arl-13(tm2322)	Mitani Lab	OIK1371
arl-13(gk513)	CGC	VC1104
osm-6(p811); mnIs17[osm-6::gfp; unc-36(+)]	Blacque Lab	SP2101

(*Continued on next page*)

Continued

REAGENT or RESOURCE	SOURCE	IDENTIFIER
mks-2(nx111); SP2101, osm-6(p811); mnIs17[osm-6::gfp; unc-36(+)]	This paper	OIK27
mks-6(gk674); SP2101, osm-6(p811); mnIs17[osm-6::gfp; unc-36(+)]	This paper	OIK340
elmd-1(syb630); SP2101, osm-6(p811); mnIs17[osm-6::gfp; unc-36(+)]	This paper	OIK154
otIs220 [gcy-5::mCherry] IV., otIs114 [lim-6p::GFP + rol-6(su1006)] I.	CGC	OH9671
kyIs128 [str-3::GFP + lin-15(+)]	CGC	CX3596
OH9671, otIs220 [gcy-5::mCherry] IV., otIs114 [lim-6p::GFP + rol-6(su1006)] I.; CX3596, kyIs128 [str-3::GFP + lin-15(+)]	This paper	OIK1278
arl-13(gk513); OIK1278, [OH9671, otIs220 [gcy-5::mCherry] IV., otIs114 [lim-6p::GFP + rol-6(su1006)] I; CX3596, kyIs128 [str-3::GFP + lin-15(+)]]	This paper	OIK1279
vuaSi24 [pBP43; Pche-11::che-11::mCherry; cb-unc-119(+)]II.; unc-119(ed3) III.; che-11(tm3433) V.	PetermanLab	EJP81
vusSi001 ocr-2:eGFP IV.	PetermanLab	EJP501
EJP81, vuaSi24 [pBP43; Pche-11::che-11::mCherry; cb-unc-119(+)]II.; unc-119(ed3) III.; che-11(tm3433) V.; +EJP501, vusSi001 ocr-2:eGFP IV.	This paper	OIK1216
arl-13(gk513); OIK1216, [EJP,81, vuaSi24 [pBP43; Pche-11::che-11::mCherry; cb-unc-119(+)]II.; unc-119(ed3) III.; che-11(tm3433) V.; +EJP501, vusSi001 ocr-2:eGFP IV.]	This paper	OIK1217
N2;nxEx1259[pbbs-8::PLC-delta PH::GFP; MKSR-2::tdTomato; coel::GFP]	Leroux Lab	MX2418
arl-13(gk513); MX2418, N2;nxEx1259[pbbs-8::PLC-delta PH::GFP;MKSR-2::tdTomato; coel::GFP]	This paper	OIK1210
ift-74(cas499[ift-74::gfp]) II.	CGC	GOU2362
bbs-5(gk537) III.; GOU2362, ift-74(cas499[ift-74::gfp]) II.	This paper	OIK997
osm-12(bbs-7)(ok1351) III.; GOU2362, ift-74(cas499[ift-74::gfp]) II.	This paper	OIK1151
hdac-6(ok3203);him-5(e1490); GOU2362, ift-74(cas499[ift-74::gfp]) II.	This paper	OIK1325
mksr-1(tm3083); GOU2362, ift-74(cas499[ift-74::gfp]) II.	This paper	OIK1147
mks-5(tm3100); GOU2362, ift-74(cas499[ift-74::gfp]) II.	This paper	OIK1220
dyf-5(ok1177) I.; GOU2362, ift-74(cas499[ift-74::gfp]) II.	This paper	OIK1205
nphp-2(gk653); GOU2362, ift-74(cas499[ift-74::gfp]) II.	This paper	OIK1221
nphp-4(tm925); GOU2362, ift-74(cas499[ift-74::gfp]) II.	This paper	OIK1150
kap-1(ok676); GOU2362, ift-74(cas499[ift-74::gfp]) II.	This paper	OIK982
klp-13(tm3737); GOU2362, ift-74(cas499[ift-74::gfp]) II.	This paper	OIK983
W07G1.5(syb722)(4X); GOU2362, ift-74(cas499[ift-74::gfp]) II.	This paper	OIK1101
FX04910, nekl-4(tm4910); GOU2362, ift-74(cas499[ift-74::gfp]) II.	This paper	OIK1215
cdkl-1(ok2694); GOU2362, ift-74(cas499[ift-74::gfp]) II.	This paper	OIK1232
cep-104(C40H1.3(tur012)(3X); GOU2362, ift-74(cas499[ift-74::gfp]) II.	This paper	OIK1263

(*Continued on next page*)

Continued

REAGENT or RESOURCE	SOURCE	IDENTIFIER
DAM297, ccep-290(tm4927) I.; GOU2362, ift-74(cas499[ift-74::gfp]) II.	This paper	OIK1334
ttll-4(tm3310); GOU2362, ift-74(cas499[ift-74::gfp]) II.	This paper	OIK1329
ttll-11(gk482); GOU2362, ift-74(cas499[ift-74::gfp]) II.	This paper	OIK1331
wdr-31(tm10423)(4X); GOU2362, ift-74(cas499[ift-74::gfp]) II.	This paper	OIK1372
F39H12.2(wdr-54)(syb1005); GOU2362, ift-74(cas499[ift-74::gfp]) II.	This paper	OIK1333
arl-13(gk513); GOU2362, ift-74(cas499[ift-74::gfp]) II.	This paper	OIK1012
osm-3(p802); GOU2362, ift-74(cas499[ift-74::gfp]) II.	This paper	OIK964
W07G1.5(rpi-1)(4X)(syb722); nphp-4(tm925); GOU2362, ift-74(cas499[ift-74::gfp]) II.	This paper	OIK1116
nphp-4(tm925); mks-5(tm3100); GOU2362, ift-74(cas499[ift-74::gfp]) II.	This paper	OIK1224
arl-13(gk513); FX04910, nekl-4(tm4910); GOU2362, ift-74(cas499[ift-74::gfp]) II.	This paper	OIK1211
hdac-6(ok3203); nphp-2(gk653); GOU2362, ift-74(cas499[ift-74::gfp]) II.	This paper	OIK1326
hdac-6 (ok3203); arl-13 (gk513); ift-74(cas499[ift-74::gfp]) II.	This paper	OIK1324
osm-3(p802); arl-13 (gk513); GOU2362, ift-74(cas499[ift-74::gfp]) II.	This paper	OIK1335
arl-13(gk513); hdac-6 (ok3203); nphp-2(gk653); GOU2362, ift-74(cas499[ift-74::gfp]) II.	This paper	OIK1327
N2; gmls13(srb-6p::GFP+pRF4)	Blacque Lab	N/A
arl-13(gk513); N2; gmls13(srb-6p::GFP+pRF4)	This paper	OIK1226
cdkl-1(ok2694); N2; gmls13(srb-6p::GFP+pRF4)	This paper	OIK1338
VC1130, ZK328.7(ift-139)(gk508) III.; N2; gmls13(srb-6p::GFP+pRF4)	This paper	OIK1296
cdkl-1(ok2694);arl-13(gk513); N2; gmls13(srb-6p::GFP+pRF4)	This paper	OIK1339
arl-13(gk513); VC1130, ZK328.7(ift-139)(gk508) III.; N2; gmls13(srb-6p::GFP+pRF4)	This paper	OIK1343
kap-1(ok676); N2; gmls13(srb-6p::GFP+pRF4)	This paper	OIK1337
bbs-8(nx77); N2; gmls13(srb-6p::GFP+pRF4)	This paper	OIK1298
ift-81(tm2355) X; N2; gmls13(srb-6p::GFP+pRF4)	This paper	OIK1344
kap-1(ok676); arl-13(gk513); N2; gmls13(srb-6p::GFP+pRF4)	This paper	OIK1336
bbs-8(nx77); arl-13(gk513); N2; gmls13(srb-6p::GFP+pRF4)	This paper	OIK1346
ift-81(tm2355) X; arl-13(gk513); N2; gmls13(srb-6p::GFP+pRF4)	This paper	OIK1300
PCP41, F16F9.3promoter::GFP + OSM-3::mCherry + rol-6	This paper	OIK1228
arl-13(tm2322); OIK1228, [PCP41, F16F9.3:: GFP + OSM-3::mCherry + rol-6]	This paper	OIK1352
W07G1.5(syb722)(4X); OIK1228, [PCP41, F16F9.3::GFP + OSM-3::mCherry + rol-6]	This paper	OIK1349
nphp-4(tm925); OIK1228, [PCP41, F16F9.3:: GFP + OSM-3::mCherry + rol-6]	This paper	OIK1351
mks-5(tm3100); N2; gmls13(srb-6p::GFP+pRF4)	This paper	OIK1299
arl-13(gk513); mks-5(tm3100); N2; gmls13(srb-6p::GFP+pRF4)	This paper	OIK1340

(*Continued on next page*)

Continued

REAGENT or RESOURCE	SOURCE	IDENTIFIER
bbs-8(nx77); mks-5(tm3100); GOU2362, ift-74(cas499[ift-74::gfp]) II.	This paper	OIK1549
arl-13(gk513); Ex[CHE-11::mcherry; ARL-13::GFP+pRF4]	This paper	OIK1547
nphp-4(tm925); W07G1.5(syb722)(4X); OIK1228, [PCP41, F16F9.3:: GFP + OSM-3::mCherry + rol-6]	This paper	OIK1350
Oligonucleotides		
C40H1.3(*cep-104*) F sgRNA 1 TCTT GTTCCTAGATGACGACATTG	Macrogen	OK625
C40H1.3(*cep-104*) R sgRNA 1 CAATGTCGTCATCTAGGAAC	Macrogen	OK626
C40H1.3(*cep-104*) F sgRNA 2 GCAGGCTGAACAGATAGCAA	Macrogen	OK627
C40H1.3(*cep-104*) R sgRNA 2 TTGCTATCTGTTCAGCCTGC	Macrogen	OK628
C40H1.3(*cep-104*) F sgRNA 3 CGACGCCGATAAGTTGGTGG	Macrogen	OK629
C40H1.3(*cep-104*) R sgRNA 3 CCACCAACTTATCGGCGTCG	Macrogen	OK630
See Table S1 for detailed oligonucleotide information.	N/A	N/A
Recombinant DNA (Plasmids)		
F16F9.3::GFP	B. Yoder Lab	PCP41
pRB1017	Addgene	59936
pDD162	Addgene	47549
OSM-3::mCherry	Hu Lab	NA
Software and algorithms		
Carl Zeiss microscope	Carl Zeiss	Axio Vert.A1
Upright fluorescence microscope	Leica	LEICA DM6 B
Electron Multiplying Charge-Coupled Devices (EMCCDs) Camera	Andor	Andor iXon (897) Ultra EMCCD (Camera)
Camera and Microscope Software	Andor	Andor iQ 3.6.2 Software
Stereo Microscope	Carl Zeiss	Stemi 508
ImageJ	Schindelin et al.[67]	https://imagej.nih.gov/ij/download.html - Version 1.53o
Workstation	HP ProDisplay P232	HP Z640 Workstation, (RAM): 160.0 GB, Processor: Intel(R) Xeon(R) CPU E5-2620 v3 2.40 GHz, 64-bit Operating System, Display resolution - 1920 × 1080 pixels
Oasis^{TM} 160 Cooling System	Andor	N/A
R Core Team	N/A	https://www.r-project.org/

EXPERIMENTAL MODEL AND STUDY PARTICIPANT DETAILS

The Nematode Growth Medium (NGM) agar plates were used to cultivate all strains generated and analyzed for this study. NGM plates seeded with *Escherichia coli* OP50 were kept at 20°C for the growth of worms. The microscope analyses were conducted using well-fed and healthy worms. The spread NGM plates were checked to see if there were adequate bacteria before the analysis day. Additionally, plates should be free of microbial and fungal contamination. If the worms starved or contaminated, they were moved to fresh NGM plates for analysis.

The key resources table contains a list of strain identifiers and genotypes.

METHOD DETAILS

CRISPR/*Cas9* in *C. elegans* and microinjection

Three sgRNAs targeting the *C. elegans C40H1*.3 (*cepr-104.1)* region are designed to generate *cepr-104.1(tur012)* allele using CHOPCHOP[68] and CRISPOR[69] online tools. The designed sgRNAs were cloned into empty RNAs into an empty sgRNA vector pRB1017 (Addgene, #59936). We confirmed the successful insertion of sgRNA through colony PCR and then proceeded to plasmid isolation. Two sgRNAs (each 40 ng/μm) were injected into the gonad parts of the wild-type worms with pDD162 (Addgene, #47549; 15 ng/μm) and pRF4 (50 ng/μm roller plasmid (rol-6)).[70] The F1 generations were followed by checking roller phenotype, and then PCR was applied to identify targeted allele generation for F1s. The DNA samples confirmed by PCR were sent to the Sanger sequencing to Macrogen. Based on the Sanger sequence results, *cepr-104.1*(tur012) mutants have 569 bp deletion, including Exon 1 and most Exon 2.

To generate double transgenics marker (pCP41, F16F9.3::GFP + OSM-3::MCHERRY + rol-6) 100 ng/μm F16F9.3::GFP, XBX-1::tdTomato (pCP41, sheath cell marker) plasmid,[50] 50 ng/μm OSM-3::mCherry (from Hu Lab, Mayo Clinic), and 50 ng/μm pRF4 (50 ng/μm roller plasmid (rol-6))[70] were mixed and injected into the gonads of the one-day adult wild-type worms.

Confocal microscopy imaging and analysis process

Cilia structure images were acquired using a Zeiss LSM900 confocal microscope maintained at a stable room temperature of 20°C. To stabilize the worms on 3% agarose pads, 2 μL of 10 mM levamisole was applied. Z-stack images were captured using the Plan ApoChromat 63x/1.40 NA objective with 0.14 μm intervals, utilizing ZEN 3 Blue edition software.

Cilia lengths were measured from the basal body to the ciliary tip for ASE and ASI cilia using the ZEN 3 Blue edition software. For PHA and PHB cilia, measurements extended from the periciliary membrane compartment (PCMC) to the ciliary tip, employing either the IFT-74::GFP or *srb-6p::gfp* markers, depending on the feasibility of generating relevant mutant strains. The categorization of PHA and PHB and ASE and ASI cilia phenotypes (cilia misdirection) was performed using ZEN 3 Blue edition software, where Z-stack images were converted into three-dimensional (3D) representations and classified as normal or cilia misdirection phenotypes.

Dendrite length measurements

Z-stack images from the cell body to the distal end of the cilia were taken to measure dendrite lengths in each mutant and wild type. Measurements were taken from the center of the cell body to the distal part of the dendrite, excluding the transition zone and cilia. Z-stack images were captured using a LEICA DM6 B compound microscope at 40X magnification, and dendrite lengths were quantified using Andor software (Andor iQ 3.6.2).

Stage analysis

Stage analysis was performed on well-fed, healthy worms. Before analysis, NGM plates were seeded with bacteria to prevent contamination and starvation. Worms were transferred to NGM agar plates for stage analysis, including larvae 1 (L1), larvae 4 (L4), and 1-day, 5-day, and 8-day adults, maintained at 20°C using a ZEISS LSM 900 confocal microscope.

QUANTIFICATION AND STATISTICAL ANALYSIS

Statistical analyses were conducted using RStudio with R programming language (version 4.1.2),[71] employing the rstatix package (version 0.7.0).[72] Plots were generated using the ggplot2 package.[73] The comparison of normal and cilia misdirection phenotypes among mutants was performed using Fisher's exact tests, while comparisons of cilia lengths, dendrite lengths, and other metrics were conducted using the Wilcoxon paired test.